Int. J. Electrochem. Sci., 15 **(2020)** 1713 – 1726, doi: 10.20964/2020.02.38

International Journal of
ELECTROCHEMICAL
SCIENCE
www.electrochemsci.org

Corrosion behaviour of X80 pipeline steel welded joint in H_2O-saturated supercritical-CO_2 environment

Yongbo Yan[1], Hongda Deng[1], Wenwen Xiao[2], Tianxiong Ou[3], Xianlong Cao[1*]*

[1] Chongqing University of Science and Technology College of Metallurgy and Materials Engineering, Chongqing 401331, China
[2] Sinopec Northwest China Petroleum Bureau, Urumqi 830011, China
[3] China Petroleum & Chemical Corporation Puguang Branch, Zhongyuan Oil Field, Dazhou 635000, Sichuan Province, China
[*]E-mail: ckffyjs@163.com , xianlong@cqust.edu.cn

Received: 22 September 2019 / *Accepted:* 27 November 2019 / *Published:* 31 December 2019

In this work, the corrosion behaviour of an X80 carbon steel welded joint in a H_2O-saturated supercritical-CO_2 (SC-CO_2) environment (40°C, 10 MPa) was studied with SEM, XRD and electrochemical techniques. The results showed that different zones (base metal (BM), fine grain heat affected zone (FHAZ), coarse grain heat affected zone (CHAZ) and weld metal (WM)) of the X80 welded joint were corroded in the SC-CO_2 environment, and $FeCO_3$ corrosion product film is formed on the surface. However, different zones exhibited different corrosion behaviours, as related to its different microstructures. The most serious zones of corrosion appeared at coarse grain heat affected zone (CGHAZ) and fine grain heat affected zone (FGHAZ), which exhibited higher proportion of pearlite. Whereas, BM and WM with higher content of ferritic were slightly corroded.

Keywords: supercritical CO_2, X80 carbon steel, welded joint, corrosion behaviour, CCS

1. INTRODUCTION

Fossil energy such as coal and oil are still the main energy source in the world today[1-3], as illustrated in Table 1. Thus, large amounts of greenhouse gas such as carbon dioxide are emitted since the current economic development is heavily dependent on fossil energy. The use of carbon capture and storage (CCS) technology can save enterprises 25% in cost[2]. Currently, CCS is the main technology to achieve reductions in carbon-intensive emissions for industries such as electricity and coal; furthermore, it is also the main choice for mitigating climate change, which is cited by major global gas emission reduction schemes[3]. To achieve the goal of limiting the temperature increase as stated from the *Paris Agreement* to "far below" 2°C, more than 2,000 CCS projects need to be

established by 2040, and there are only 17 CCS projects which are currently in operation (up to 2017)[2,4]. CCS has been operated in Europe, America and other regions for many years, and projects in Asia, Africa and other countries such as China and Japan are gradually starting to be established and operated rapidly.

Table 1. Energy composition of the United States, China and the world in 2016

Energy composition	United States		China		Global	
	Oil equivalent 10^8/t	Proportion/%	Oil equivalent 10^8/t	Proportion/%	Oil equivalent 10^8/t	Proportion/%
Oil	8.631	37.98	6.443	19.56	15.573	14.95
Natural gas	7.163	31.52	3.095	9.40	32.041	30.76
Coal	3.584	15.77	19.329	58.68	37.320	35.83
Nuclear energy	1.918	8.44	0.554	1.68	5.921	5.68
Hydropower	0.592	2.60	2.646	8.03	9.103	8.74
Regenerable	0.838	3.69	0.871	2.64	4.196	4.03
Total	22.726	100.00	32.938	100.00	104.154	100.00

In CCS, SC-CO_2 is the best transport phase of CO_2 because of its excellent transport and flow characteristics and is widely used in actual production abroad[5]. Pipeline transportation of supercritical CO_2 is considered as a more economical and reliable transportation method[6]. At present, SC-CO_2 pipelines are still transported by carbon steel pipes[7]. A comparative analysis shows that the corrosion rate rating of carbon steel materials such as X70 is high in a SC-CO_2 environment. The service environment in production operations is far more complex than the experimental environment, and there exist high risk of pipeline leakage and other failure problems. According to statistics, the frequency of CO_2 leakage per 1000 km of pipeline is 0.32, which is much higher than that of oil and gas pipelines, which is 0.17[7].

Sewed steel pipelines (straight seam steel pipes and spiral steel pipes) are often used in pipeline construction, and also connected by welds. However, the uneven heating of a welded joint caused by the welding thermal cycle difference will lead to more serious corrosion, which will directly lead to safety accidents such as pipeline leakage, furthermore damage and even personal injury[8-9]. According to the reports, most leakage accidents of CO_2 pipelines are caused by corrosion and welding. [10-12] At present, the research on the corrosion of welded joints mainly focuses on that occurred in conventional environments, such as soil, aqueous solution, NaCl solution and simulated seawater. There is little research on the corrosion of welded joints in SC-CO_2 environments. It is

becoming more urgent to study the corrosion of welded joints in a SC-CO_2 environment due to the demand in the future from transportation of SC-CO_2 in CCS.

In this study, an X80 pipe welded joint consisted of base metal (BM), fine grain heat affected zone (FGHAZ), coarse grain heat affected zone (CGHAZ) and weld metal (WM) was used as the research object. The corrosion of different zones of the welded joint in the SC-CO_2 environment containing saturated water was studied with an electrochemical techniques and SEM and XRD. The results can provide a theoretical basis and supporting data for corrosion protection at the welded joint of a SC-CO_2 pipeline. This is of great significance for reducing the risk of leakage in the welded joint zone of a SC-CO_2 pipeline and improving the safety and integrity of the pipeline.

2. EXPERIMENTAL

2.1 Material and method

The welded joint of X80 pipeline steel was selected as the test material in this research. First, the welded joint was cut into a 20-mm wide block sample along the welding direction. Then, the welded sample splices were then ground using 240, 600, 1000, 1200, 1500 and 2000 grit silicon carbide sand papers, followed by polishing with 1μm diamond suspension abrasive. Finally, the polished surface was corroded with a 4% nitric acid alcohol solution. The treated specimen is shown in Fig. 1. In addition, the boundary lines between BM and FGHAZ, FGHAZ and CGHAZ, and CGHAZ and WM could be clearly seen in Fig. 1. The sheet specimens of the WM, CGHAZ, FGHAZ and BM were obtained by a wire cutting method where the sample was cut along the boundary line at the central position of each zone. The sliced samples were identified and calibrated by an optical metallographic microscope (OLYMPUS, QX71) to ensure that the exposed surface was completely the required target zone.

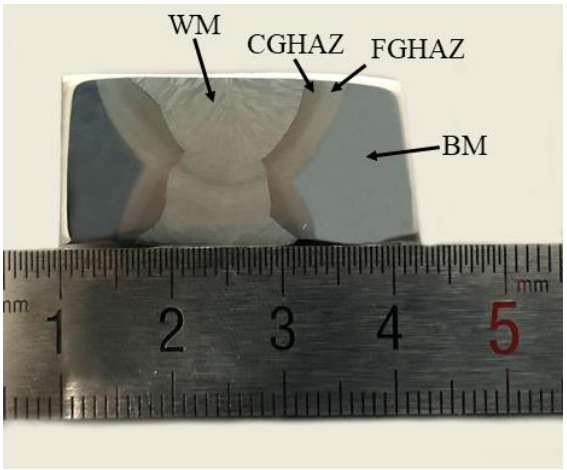

Figure 1. Distribution zones of the X80 carbon steel welded joint.

The identified sheet specimen was cut into a sample with a size of 4 mm × 5 mm ×1 mm by a wire electric discharge machine. All the specimens were degreased and then rinsed with deionized water and acetone before epoxy pouring. After that, the specimens were placed in a silicone mould to make its exposed area 20 mm^2, and the remaining faces were sealed with epoxy resin. Five immersion test specimens were prepared for each zone, so a total of 20 test modules were required for these four zones. The specimens of each zone were sanded with abrasive paper from stage to stage (240, 600, 1200), washed with deionized water, wiped with acetone, blown with cold air, and then stored under vacuum before the immersion corrosion test.

2.2 Immersion corrosion experiment

The immersion corrosion experiment was tested in a *Cortest* 5 L high-pressure autoclave with a pressure of 10 MPa at 40°C for 120 h. Before the corrosion test, 1 L deionized water was added into the autoclave, then the samples were quickly placed inside and installed. Next, the autoclave was sealed, and then it was deoxygenated for 6 h by passing high purity N_2 (99.99%) through the apparatus to ensure that the SC-CO_2 was saturated with H_2O throughout the test. The timing was started after the temperature and pressure was raised to the required stable conditions for 3 h. All immersion corrosion tests were performed under static conditions. Four samples were taken from each zone for the immersion corrosion test.

2.3 Electrochemical measurements

Electrochemical workstation (CHI 660E) was applied to carried out electrochemical corrosion tests on the sample by using a three-electrode system in a 3.5% NaCl aqueous solution at 40°C under ambient pressure. The samples of the different zones before and after were corroded in SC-CO_2 were used as the working electrode (WE), a platinum electrode was the counter electrode (CE), and a Ag/AgCl electrode (3.5 M KCl) was the reference electrode (RE). The open circuit potential (OCP) measurements were taken over a 3600s duration of continuous monitoring. The polarization curve measurements were performed when the OCP fluctuation was less than 0.5 mV/min. The polarization curve measurements were performed from -250 mV to 250 mV vs. OCP with a scan rate of 0.5 mV/s.

2.4 Structural analysis of corrosion products

The organization of the structure, corrosion morphology, and corrosion product compositions of the sample were analysed by means of scanning electron microscopy (SEM) and X-ray diffractometry (XRD).

3. RESULTS

3.1 Analysis of the welded joint microstructures

An optical microscope (OM) was used to examine the microstructures of the X80 carbon steel welded joint, including the BM, FGHAZ, CGHAZ, and WZ, as shown in Fig. 2. Fig. 2a shows that the BM microstructure is composed of polygonal ferrite (PF) and quasi-polygonal ferrites (QF), and there are a large number of finely granular M-A islands diffused in the interior and along the grain boundaries of the QF.

Fig. 2b shows the metallographic microstructure of the FGHAZ. The FGHAZ structure mainly consists of pearlite (P), a small amount of QF and a very small amount of PF. Additionally, it contains a small amount of fine M-A islands. The FGHAZ is obtained by slow cooling after the temperature reaches 1000°C during the welding process.

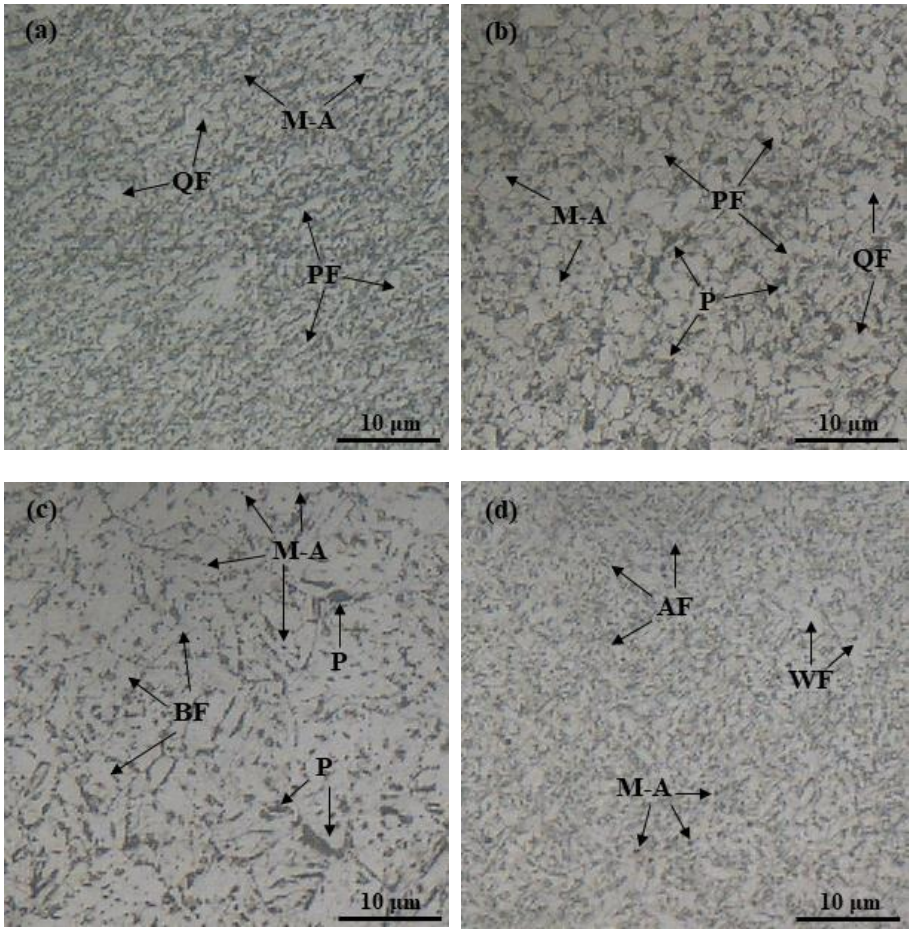

Figure 2. OM morphologies of different zones in the X80 carbon steel welded joint: (a) BM, (b) FGHAZ, (c) CGHAZ, and (d) WZ.

As shown in Fig. 2c, the structure of the CGHAZ consists of P and bainite ferrite (BF), and the M-A islands are distributed at the lath of the BF. The temperature in this zone can reach above 1300°C during the welding process, which leads to its thick grain size and extremely uneven distribution. The transformation mechanism of BF is a shear and diffusion mixed phase transition [13], which has a high

dislocation density. The microalloy compound, nitride, and carbide are dissolved since the CGHAZ is heated to a higher austenitizing temperature during the welding process, resulting in an obvious increase in grain size.

As shown in Fig. 2d, the structure of the WZ consists of acicular ferrite (AF) and a very small amount of widmanstatten ferrite (WF). In addition, the WM contains a small number of M-A islands.

The acicular ferrite is an intragranular nucleated ferrite intermingled and induced by a nonmetal in the weld metal. The grain boundary is distributed at a small angle with a large dislocation density.

3.2 XRD analysis

Fig. 3 shows the XRD test results of each zone sample of the X80 carbon steel welded joint after corrosion for 120 h in a H_2O-saturated SC-CO_2 phase.

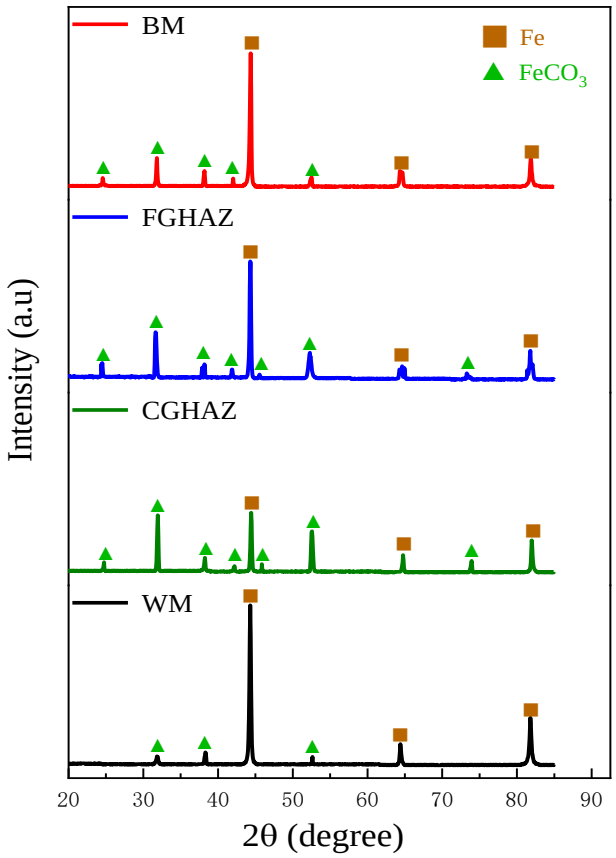

Figure 3. XRD of the X80 carbon steel welded joint after corrosion for 120 h in a H_2O-saturated SC-CO_2 phase

The analysis results show that there are obvious Fe and $FeCO_3$ phases for corrosion scale formed on the surface of each sample after corrosion. This shows that the corrosion products of the sample in a SC-CO_2 environment is $FeCO_3$, which is the same as that in an ordinary CO_2 environment for carbon steel[14]. The intensity of Fe and $FeCO_3$ peaks on the surface of the 4 zone specimens are

different, which may be caused by the different coverage situation on the sample surfaces by $FeCO_3$ generated from the corrosion. The stronger the intensity of the $FeCO_3$ peak, the more $FeCO_3$ product formed on the surface of the specimen. As shown in Fig. 3, the strongest $FeCO_3$ peak on the sample surface of the four zones is the CGHAZ, followed by that of the FGHAZ; there is not much difference of peak intensity between the BM and the WM. This indicates that the thickest layer of $FeCO_3$ generated by corrosion on the sample surface is with the CGHAZ, the FGHAZ has the second thickest layer, and then there is just a few $FeCO_3$ formed on the BM and the WM.

3.3 Corrosion morphology

Fig. 4 shows the SEM surface morphology of each zone specimen of the X80 welded joint corroded in the CO_2 phase of the SC-CO_2 for 120 h. As seen from Fig. 4, flake-like $FeCO_3$ crystals were adsorbed on the surface of each sample. The coverage of $FeCO_3$ on the sample surface of different zones is different, which may be related to the microstructures difference at different zones. The $FeCO_3$ formed at BM (Fig. 4a, 4b), FGHAZ (Fig. 4c, 4d), and WM (Fig. 4g, 4h) are distributed independently in an island shape. It is not shown any thick and continuous corrosion product layer overlying their surface. $FeCO_3$ island on the surface of the FGHAZ is larger, and the $FeCO_3$ islands in the BM and the WM are more but with smaller size. In addition, there is a flat and continuous $FeCO_3$ film on the surface of the specimen outside of the island. As shown in Figures 4e and 4f, the CGHAZ samples were most severely corroded among zones of the welded joint. The $FeCO_3$ islands was resulted from the corrosion to form a polycrystalline multilayer crystalline film, which covers almost completely on the sample surface.

However, there are a large number of pores on both the $FeCO_3$ islands on the sample surface of each zone. The surface of the polycrystalline $FeCO_3$ film becomes the potential initiation location of local corrosion.

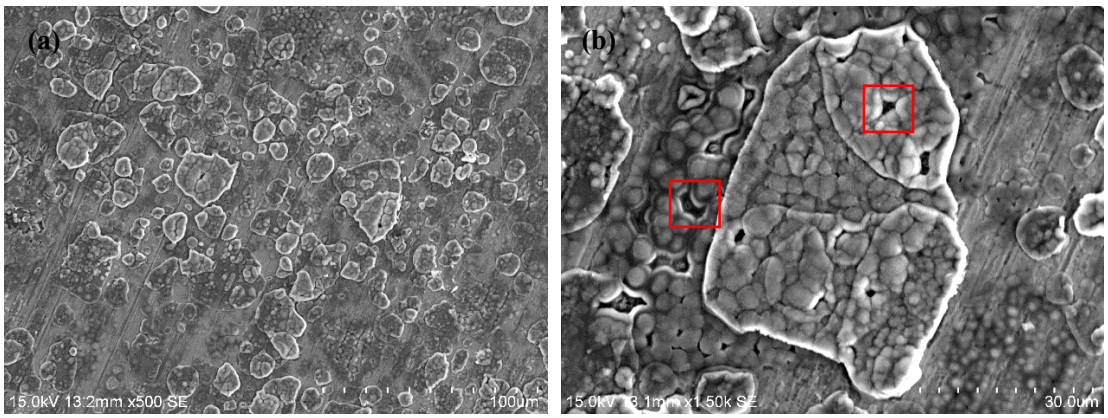

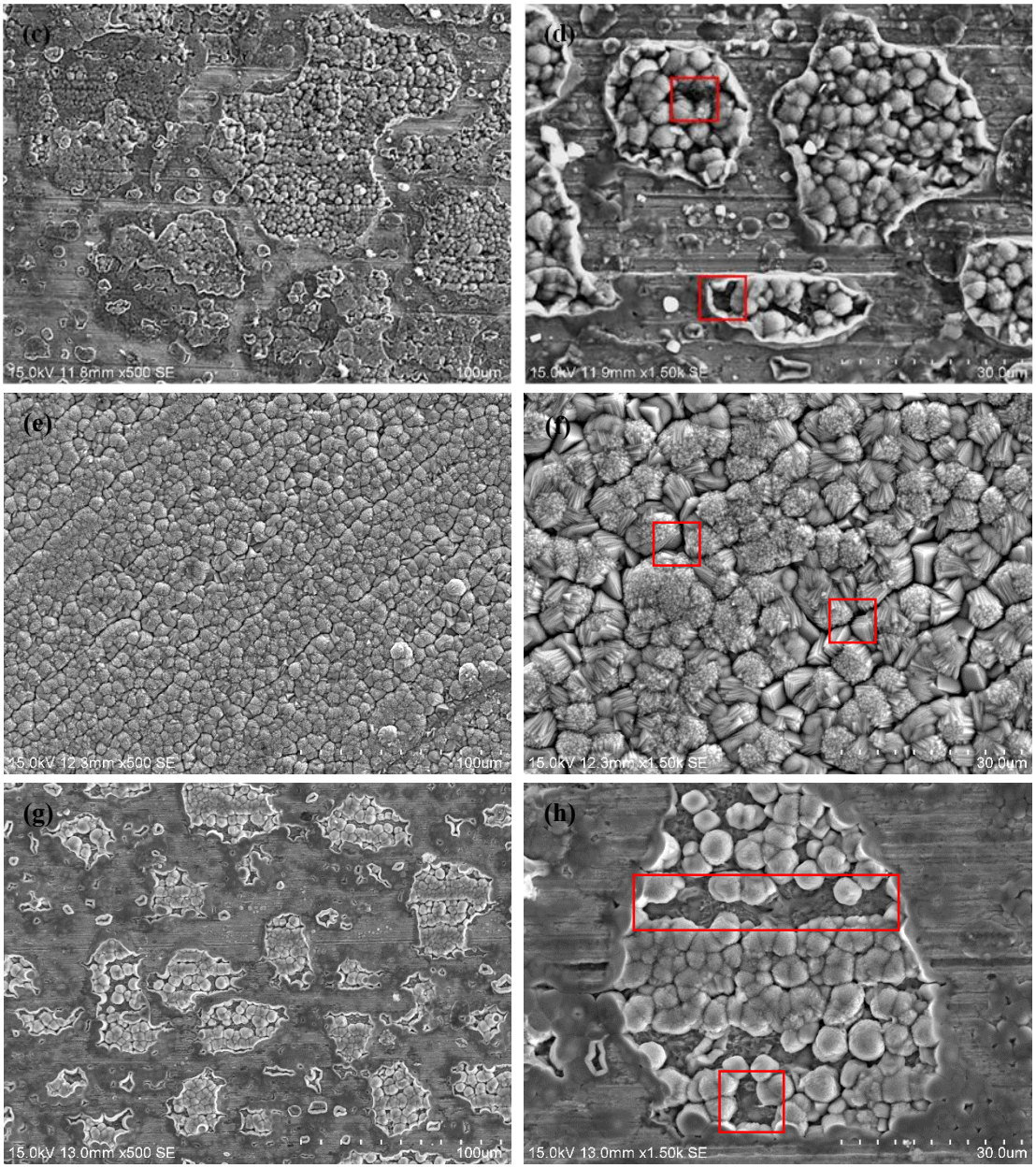

Figure 4. SEM surface morphologies of the X80 carbon steel welded joint after corrosion in a H_2O-saturated SC-CO_2 phase for 120 h: (a and b) BM, (c and d) FGHAZ, (e and f) CGHAZ, and (g and h) WM.

3.4 Open circuit potential

Figure 5 shows the OCP variation graphs for each zone of the welded joint in a 3.5% NaCl aqueous solution before and after corrosion in SC-CO_2, along with the corrosion time. As shown in Fig. 5a and 5b, the OCP of each zone of the welded joint before and after corrosion decreased with time in the 3.5% NaCl aqueous solution, and the OCP of CGHAZ decreased the most. The OCP tends to be stable after immersion for 1 h. The OCP of CGHAZ was the lowest, following by that of the FGHAZ, BM and WM. Thus, the FGHAZ and the BM are the second highest, and the WM has the

highest OCP. In addition, the OCP of the samples of each zone is higher than that before corrosion. It shows that the corrosion product film ($FeCO_3$) formed by corrosion of the X80 welded joint in an SC-CO_2 environment has a certain protective effect on the metal matrix.

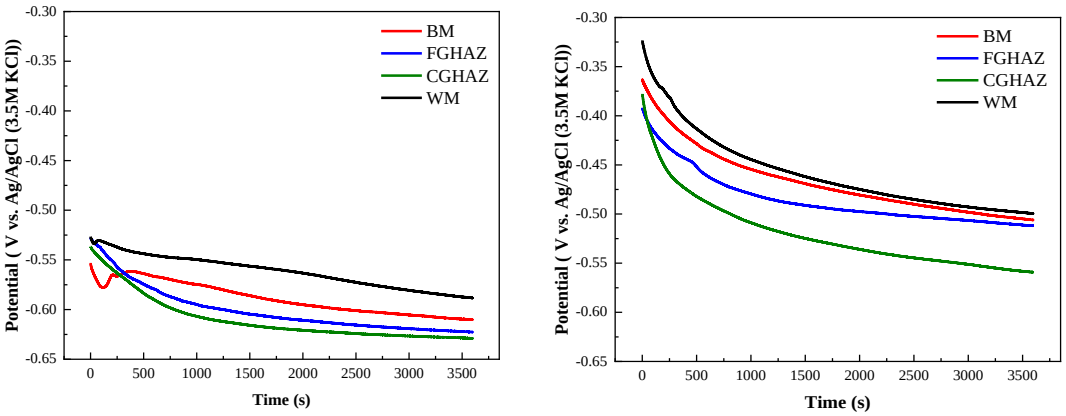

Figure 5. Time dependence of OCP with the X80 carbon steel welded joint before (a) and after (b) SC-CO_2 corrosion in a 3.5% NaCl aqueous solution.

3.5 Polarization curve measurements

Fig. 6 shows the polarization curves of the four zones in the X80 carbon steel welded joint before and after SC-CO_2 corrosion in a 3.5% NaCl aqueous solution. It can be seen from Fig. 6a that the reaction of the four regions in the 3.5% NaCl aqueous solution before the SC-CO_2 corrosion were controlled under active polarization. Fig. 6b shows that passivity appeared in the zone curves after corrosion in a H_2O-saturated SC-CO_2 phase in 3.5% NaCl solution. This is because the metal samples have generated a protective $FeCO_3$ film on their surface after corrosion in the SC-CO_2 environment. The $FeCO_3$ film breaks at a higher polarization potential[15]. As the $FeCO_3$ generated on different zones corroded in the SC-CO_2 environment have different film microstructure, different zones show different degrees of passivation. As for different zones after corroded, the passivation of the CGHAZ and the FGHAZ is stronger than that of the BM and the WM. However, as a whole, the passivation phenomenon caused by the existence of $FeCO_3$ film is weak.

Table 2 shows the results of the polarization curve parameter fitting of the samples in each zone before and after SC-CO_2 corrosion in a 3.5% NaCl solution. The fitting results were obtained by a Tafel curve extrapolation. According to the corrosion current density (I_{corr}) in the fitting result the corrosion rate is calculated by formula (1). It can be seen from the fitting results that the corrosion potential (E_{corr}) of the samples in each zone after corrosion in the SC-CO_2 environment is lower than that before corrosion, and the I_{corr} is higher than that before corrosion. This shows that although the $FeCO_3$ film formed on the surface of the metal sample has a slight protective effect, there may be more holes and gaps on the surface of the film, which is a potential danger for inducing local corrosion.

$$V(mm/a) = \frac{0.00327 \times I_{corr}\,(\mu A/cm^2) \times A}{n \times D(g/cm^3)} \qquad (1)$$

Where *V* represents the corrosion rate for the metallic material, *A* represents the atomic mass of the reactant, *n* represents the number of electrons gained or lost, and *D* represents the density of the metal materials. In this work, *A* takes the atomic weight of Fe, which is 55.8. *D* takes the ordinary carbon steel density value of 7.8 g/cm^3.

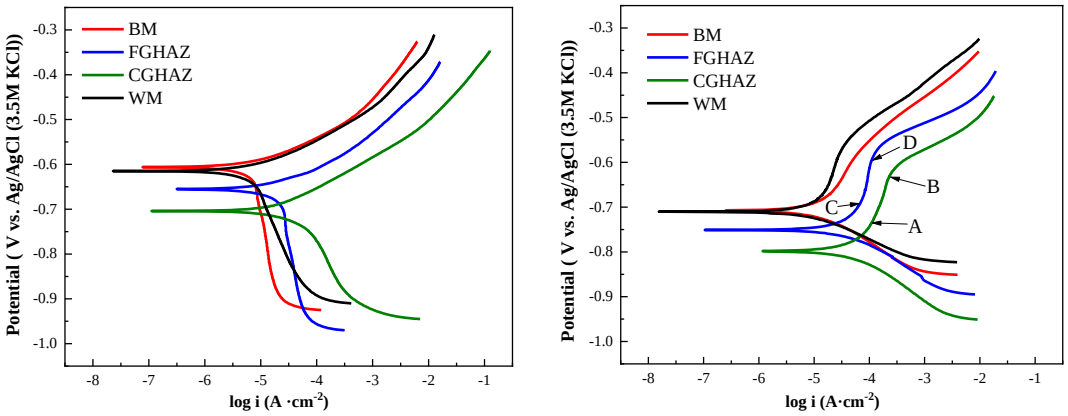

Figure 6. Polarization curves of the X80 carbon steel welded joint before (a) and after (b) SC-CO_2 corrosion in a 3.5% NaCl aqueous solution.

Table 2. Fitted electrochemical parameters of the polarization curves of the X80 carbon steel welded joint before (a) and after (b) SC-CO_2 corrosion in a 3.5% NaCl aqueous solution

Condition	Zone	E_{corr} (V vs. Ag/AgCl (3.5 M KCl))	I_{corr} (μA/cm^{-2})	Corrosion rate (mm/a)	Corrosion level（NACE RP0775-2005）
Before the corrosion	BM	-0.606	9.77	0.114	Moderate
	FGHAZ	-0.655	28.4	0.332	Extremely serious
	CGHAZ	-0.704	35.5	0.414	Extremely serious
	WM	-0.615	8.59	0.100	Moderate
After the corrosion	BM	-0.707	13.7	0.160	Serious
	FGHAZ	-0.750	50.6	0.592	Extremely serious
	CGHAZ	-0.798	62.3	0.729	Extremely serious
	WM	-0.711	10.6	0.124	Moderate

4. DISCUSSION

The corrosion behaviour of the X80 welded joints in a SC-CO_2 environment is the same as that in other H_2O-saturated CO_2 phase environments[16]. When carbon steel is in a H_2O-saturated supercritical-CO_2 environment, even if the metal is in the SC-CO_2 phase, there is still a free water film

precipitated by condensation on its surface[17]. The CO_2 in the environment combines with this free water to form carbonic acid, which causes corrosion on the surface of the metal base. In addition, the water film deposited on the metal surface is supersaturated because the water solubility of supercritical CO_2 is extremely small. According to a model calculation[18] of the pH value of supercritical CO_2, the pH of a H_2O-saturated SC-CO_2 environment is approximately 3. The corrosion mechanism of the X80 welded joint is the same as that of X70 and other carbon steel materials in a H_2O-saturated SC-CO_2 environment, which is an electrochemical reaction. The reaction principle is[19]:

First, CO_2 dissolves in H_2O to form carbonic acid:

$$H_2O\ (l) + CO_2\ (g) \Leftrightarrow H_2CO_3\ (aq) \quad (2)$$

Then, the carbonic acid will react in the water to cause an ionization reaction, which releases H^+, HCO_3^-, and CO_3^{2-}:

$$H_2CO_3\ (aq) \Leftrightarrow HCO_3^- + H^+ \quad (3)$$

$$HCO_3^- \Leftrightarrow CO_3^{2-} + H^+ \quad (4)$$

As the pH value of the H_2O-saturated SC-CO_2 environment is low and at approximately 3, the cathode reaction acts as a reducing agent for H^+ produced by a secondary ionization of carbonic acid and that is how the direct hydrogen evolution reaction occurs[20].

$$2H^+ + e^- \Longrightarrow H_2 \quad (5)$$

The anodic reaction is the dissolution reaction of the carbon steel in an acidic solution:

$$Fe \Longrightarrow Fe^{2+} + 2e^- \quad (6)$$

Therefore, the total corrosion reaction equation of carbon steel in a H_2O-saturated SC-CO_2 environment is:

$$Fe + H_2CO_3 \Longrightarrow Fe^{2+} + CO_3^{2-} + H_2 \quad (7)$$

In this work, during the actual corrosion of the CO_2 phase in a H_2O-saturated SC-CO_2 environment, there will be extremely uneven condensed water deposited on the surface of the metal. The condensed water will first adsorb to the metal surface in tiny droplets to cause electrochemical corrosion. Meanwhile, the metal at the droplet is used as a cathode, and the nearby metal is used as an anode, so the $FeCO_3$ formed by the reaction is adsorbed around the reaction site. These $FeCO_3$ grains will provide a nucleation site for the $FeCO_3$ generated by subsequent reactions. In addition, the $FeCO_3$ generated by subsequent corrosion will precipitate and grow along this location. However, there are large holes and gaps among these $FeCO_3$ grains (as shown in Fig. 3), and the electrolyte in the corrosive environment can enter into the pores and reach the metal surface. The anode zone is only a small metal matrix in the pores and is much smaller than that of the cathode zone, which results in a sharp increase of the corrosion rate and causes severe corrosion unevenly distributed in local regions.

Due to the non-uniformity of the microstructure of the metal material, accelerated corrosion dissolution at a local location is caused[21-23]. Kobayashi's research found that the corrosion-resistant area of the HAZ in the pipeline welded joint is much lower than the tube BM [24]. Also, the HAZ acts as an anode region for galvanic corrosion, and the corrosion rate will corrode faster than the weld zone and the substrate zone[25]. In this work, the corrosion specimens of the different zones are quite different in the SC-CO_2 environment, which is related to the difference in metallographic structure of each zone[26]. According to the research conclusions of Wang et al. [27], a Kelvin potential was measured in the X80 simulated welded joint region. It was found that a structure composed entirely of

pearlite had the lowest Kelvin potential (about -0.78 V to -0.49 V), which slightly increased when ferrite was doped in the structure (about -0.49 V to -0.42 V). Moreover, as shown in formula (8), the composition of ferrite has the highest Kelvin potential (about -0.42 V to -0.27 V). Thus, the self-corrosion potential E_{corr} of the material is proportional to the Kelvin potential in a corrosive environment[28-29].

This indicates that in the structure of the X80 welded joint, the corrosion potential of ferrite is higher than that of pearlite, and the doping of ferrite in pearlite can enhance the corrosion potential of the material.

$$E_{corr} = \left(\frac{W_{ref}}{F} - \frac{E_{ref}}{2}\right) + \varphi \qquad (8)$$

where W_{ref} represents work function for the reference electrode, $\frac{E_{ref}}{2}$ represents the half-cell potential of the reference electrode, F represents the Faraday constant, and φ represents the Kelvin potential.

Comparing the various zone structures of the X80 welded joint in this test, it is found that the CGHAZ is dominated by a pearlite and bainitic ferrite, which contain a coarse grain. The corrosion potential of the pearlite is lower than that of the other structures in the corrosive environment. In addition, the coarse grains further reduce the corrosion potential of the CGHAZ, which makes it have a large corrosive tendency. The FGHAZ is mainly composed of P with a low corrosion potential and also contains QF and PF. The corrosion potential of the FGHAZ can be appropriately increased as these two kinds of ferrite are doped into the pearlite, which also lowers the corrosion tendency. The BM is mainly composed of ferrite structures such as PF and QF, and the WM is mainly AF.

As both of these regions are mainly composed of ferrite structure with higher corrosion potential, and with no pearlite of lower corrosion potential among them, the corrosion potentials of the BM and the WM are higher than those of the FGHAZ and CGHAZ, and their corrosion tendencies are the least of all.

5. CONCLUSIONS

(1) In an X80 welded joint, the BM is composed of polygonal ferrite (PF) and quasi-polygonal ferrite (QF), and there are a large number of fine granular M-A islands distributed in the interior and along the grain boundaries of the QF. The FGHAZ structure consists of pearlite (P), a small amount of QF and PF, and contains a small number of fine M-A islands. The CGHAZ is composed of P and bainitic ferrite (BF), and a small number of M-A islands are distributed at the lath of the BF. In addition, the crystal grains of the CGHAZ are coarse. The WM structure consists of acicular ferrite (AF) and a very small amount of widmanstatten ferrite (WF), which also contains a small number of M-A islands.

(2) There is a big difference in the corrosion conditions among the various regions of the X80 welded joint in the H_2O-saturated SC-CO_2 environment (40°C, 10 MPa). The most severely corroded zone is the CGHAZ, followed by that of the FGHAZ, and then the WM and BM.

(3) The microstructure differences of the different zones in the X80 welded joint lead to differences in the corrosion degree. More serious corrosion occurred in the SC-CO_2 environment when pearlite accounted for the majority phase of the X80 carbon steel (such as that of the CGHAZ). Less corrosion happened as the ferrite content of the X80 carbon steel increased (such as that of the FGHAZ). The corrosion in the SC-CO_2 environment was relatively slight when the ferrite accounts for the majority phase in the X80 carbon steel (such as that of the BM and WM).

ACKNOWLEDGEMENTS
The authors would like to acknowledge the financial support from the Research Foundation of Chongqing University of Science & Technology (CK2016Z09), the Natural Science Foundation Project of CQ CSTC (cstc2019jcyj-msxmX0181 & cstc2019jcyj-msxmX0188) and the Transfer Program of Institutions of Higher Education in Chongqing (KJZH17136).

References

1. X. D. Fu, Y. B. Wang, X. G. Bi, Y. R. Lu, J. H. Liang, and W. Y. Guo, *Nat. Gas Oil*, 35 (2017) 8.
2. P. Andrews-Speed and S. Zhang, *China as a Global Clean Energy Champion*, (2019) Palgrave Macmillan, Singapore.
3. Y. Song, M. Zhang and R. F. Sun, *Energy Policy*, 132 (2019) 167.
4. Danish, M. A. Baloch, N. Mehmood and J. W. Zhang, *Sci. Total Environ.*, 678 (2019) 632.
5. B. Chen, H. L. Xiao and S. G. Cao, *Nat. Gas Chem. Ind.*, 42 (2017) 63.
6. G. A. Jacobson, S. Kerman and Y. S. Choi, *Mater. Perform.*, 53 (2014) 24.
7. J. Gale and J. Davison, *Energy*, 29 (2004) 1319.
8. Y. Tang, X. P. Guo and G. A. Zhang, *Corros. Sci.*, 118 (2017) 118.
9. R. Cao, Y. Ding, X. K. Zhao and W. Q. Zhong, *Corros. Sci. Prot. Technol.*, 29 (2017) 657.
10. Y. D. Li, X. Tang, Y. Li, *Mater. Rev.*, 31 (2017) 158.
11. R. Bongartz, J. Linssen and P. Markewitz, *Carbon Capture, Storage and Use: Technical, Economic, Environmental and Societal Perspectives*, (2015) Springer International Publishing, Switzerland.
12. R. Barker, Y. Hua and A. Neville, *Int. Metall. Rev.*, 62 (2017) 1.
13. D. G. Yu, Y. R. Zhu and D. J. Chen, *Acta Metall. Sinica*, 30 (1994) 385.
14. K. W. Gao, F. Yu, X. L. Pang, G. A. Zhang, L. J. Qiao, W. Y. Chu and M. X Lu, *Corros. Sci.*, 50 (2008) 2796.
15. B. Wang, T. Xin and Z. Gao, *Int. J. Electrochem. Sci.*, 12(2017) 7205.
16. Y. C. Zhang, X. L. Pang, S. P. Qu, X. Li and K. W. Gao, *Corros. Sci.*, 59 (2012) 186.
17. Y. S. Choi and S. Nesic, *Int. J. Greenh. Gas. Con.*, 5 (2011) 788.
18. L. Wei, X. L. Pang and K. W. Gao. *Acta. Metall. Sin.*, 51 (2015) 701.
19. C. Sun, J. B. Sun, Y. Wang, X. Q. Lin, X. D. Li, X. K. Cheng and H. F. Liu. *Corros. Sci.*, 107 (2016) 193.
20. S. Nesic. *Energ. Fuel*, 26 (2012) 4098.
21. J. L. Albarran, L. Martinez and Lopez H F. *Corros. Sci.*, 41 (1999) 1037.
22. J. T. Bulger, B. T. Lu and J. L. Luo. *J. Mater. Sci.*, 41 (2006) 5001.
23. R. A. Carneiro, R. C. Ratnapuli and V. F. C. Lins. *Mater Sci Eng*, A357 (2003) 104.
24. Y. Kobayashi, K. Ume, T. Hyodo and T. Taira. *Corros. Sci.*, 27 (1987) 1117.
25. Z. Fan, J. Y. Liu, S. L. Li and T. J. Zhang. *J. Southwest Petro Univ (Sci Technol Ed)*, 31 (2009) 171
26. F. F. Eliyan and A. Alfantazi. *Corros. Sci.*, 85 (2014) 380.

27. L. W. Wang, C. W. Du, Z. Y. Liu, X. X. Zeng and X. G. Li. *Acta. Metall. Sinica.*, 47 (2011) 1227.
28. M. Stratmanm, *Corros. Sci.*, 27 (1987) 869.
29. M. Stratmanm, H. Streckel and B. Bunsen, *Phys. Chem.*, 92 (1988) 1244.